Chaotic Mixing of Shear-Thinning Fluids

Thomas C. Niederkorn and Julio M. Ottino
Dept. of Chemical Engineering, Northwestern University, Evanston, IL 60208

This article investigates the effect of shear-thinning viscosity on chaotic mixing when the kinematics first begin to deviate from Newtonian flow. Computations are done for a 2-D, time-periodic flow between eccentric cylinders. The effectiveness of mixing is analyzed by examining the asymptotic coverage of a passive tracer, character and location of periodic points, and the rate of stretching of fluid elements. Small variations in the velocity field associated with non-Newtonian kinematics produce large effects in the chaotic advection of a passive tracer. The stretching rate remains exponential, but with a long time constant as the shear-thinning effect increases, often resulting in the birth of new periodic islands and a decrease in the asymptotic coverage of the tracer. Exceptions to these observations are possible: both the stretching rate and the asymptotic coverage might increase as shear thinning increases. Results also indicate that suitable manipulation of operating conditions can produce shear-thinning flows which mix as well as Newtonian flows. Since significant effects are observed with less than a 4% difference in the velocity fields, the assumption of Newtonian kinematics can lead to large errors in the design and operation of process mixing equipment for non-Newtonian fluids.

Introduction and Background

Non-Newtonian fluids are common in a variety of industrial applications such as polymer processing, biochemical engineering, and consumer products. A key consideration in the processing of these fluids is an understanding of what design variables lead to the most efficient fluid mixing (Middleman, 1977; Tadmor and Gogos, 1979; Rauwendaal, 1991; Harnby et al., 1992). Such an understanding, however, is currently lacking. In fact, the current practice of designing industrial mixers for complex fluids is more art than science. Design procedures often depend heavily on empiricism with little fundamental understanding of the underlying fluid mechanics. This is true especially for non-Newtonian flows as the design problem contains a two-fold complexity: complicated geometries such as tank and impeller systems and twin-screw extruders as well as complicated fluid rheology such as elasticity and a deformation-rate-dependent viscosity. Thus, previous studies of laminar mixing in the context of polymer processing have focused on simplifying both the kinematics and the geometry. For example, the single-screw extruder has been modeled as the combination of the flow in a driven rectangular cavity and the axial flow in the annulus of rotating concentric cylinders (Ottino and Chella, 1983). Recent advances in finite-element methods have allowed simulations in complicated two-dimensional geometries (for example, kneading discs in Lawal et al., 1993); however, Newtonian kinematics are often assumed even if the materials are manifestly non-Newtonian.

Despite the ubiquity of non-Newtonian flow, it is apparent that there is a dearth of systematic studies of mixing in well characterized flows. A few articles have nevertheless addressed this difficult problem (for a review, see Nienow and Elson, 1988), and the bulk of these research articles have concentrated on mixing times and power consumption.The first of this kind is the one by Metzner and Otto (1957), which focuses on adapting the existing power number—Reynolds number correlation curves by use of an apparent viscosity. Other representative studies including those by Godleski and Smith (1962), Hall and Godfrey (1970), Ford and Ulbrecht (1976), and Carreau et al. (1992), extend this initial study to systems with a non-constant flow index, different geometries, and elastic fluids.

The underlying theme of these studies is a focus on macroscopic aspects of the flow. By contrast, the goal of this article (and a recent one by Niederkorn and Ottino, 1993, on an elastic fluid) is to address the importance of rheology on detailed

Present address of T. C. Niederkorn: The Procter & Gamble Company, Este Process Technology Center, Cincinnati, OH 45232.

mixing structures in simple, but well characterized, flows. The flows selected for these studies are two-dimensional chaotic flows between eccentric cylinders. There are several reasons for this choice. These types of flows are controllable and experimental verification is possible. There is also a body of theory available which allows for the analysis of key aspects of the mixing characteristics. This article first discusses some principles of chaotic mixing and the selected flow geometry, as well as the rheological model, computational methods used to simulate the flow, and the techniques used to analyze chaotic mixing. Then, the consequences of shear-thinning behavior in both counterrotating and corotating operation are discussed.

Chaotic mixing

In the context of this study, we refer to mixing as the distribution of a passive tracer throughout a bulk fluid. This can be quantified as a decrease in the average striation thickness of the tracer or equivalently the generation of intermaterial area between the tracer and the bulk fluid. The goal is to reduce the striation thickness as quickly as possible such that the driving force for molecular diffusion is increased. The tracer will then become completely mixed once the diffusion mechanism is completed. This operation is commonly referred to as blending in the industrial community.

In this section, we introduce briefly some of the key concepts in chaotic mixing. A more thorough review of these issues can be found in Ottino (1990). It is now well known that if a two-dimensional velocity field is steady, the velocity field is integrable, and the system is nonchaotic (Aref, 1984). If a tracer is injected into the flow, it will follow the closed streamlines and the mixing is poor since the tracer will only travel through a limited portion of the flow domain. More importantly, the rate of stretching in steady flow is linear in time resulting in a linear rate of intermaterial area generation.

If, however, the two-dimensional velocity field is made time-periodic, there is a good chance that the system will possess chaotic trajectories. Fluid elements are no longer trapped by closed steady streamlines and are free to wander throughout the chaotic flow domain. Also, the rate of stretching is exponential in the chaotic region resulting in a much faster rate of intermaterial area generation. Consequently, in two dimensions, a time-periodic flow mixes more efficiently than a steady flow. It should be noted that a three-dimensional *steady* flow can produce chaotic trajectories.

The basic structure in a time-periodic flow is determined by the location of periodic points. The periodic points are classified into two groups, elliptic or hyperbolic, depending on the nature of the deformation in the neighborhood of the material point. Fluid rotates in the neighborhood of an elliptic periodic point and the rate of stretching is linear; elliptic points are often found in the center of islands. Since a passive tracer is trapped inside an island, these regions are an obstacle to mixing. Hyperbolic periodic points, on the other hand, are associated with the chaotic regions. In the neighborhood of these points, the fluid is compressed in one eigendirection and stretched in the other eigendirection. The continuation of these regions constitutes the manifolds of the flow.

There have been many experimental studies of chaotic advection in two-dimensional, time-periodic flows (for a recent review, see Ottino et al., 1992). They all focus on Newtonian fluids except for the recent study of a viscoelastic fluid by Niederkorn and Ottino (1993) and a short experimental study by Leong and Ottino (1990). In the Newtonian case, the dye structure is independent of the velocity of the moving boundaries. For example, in the case of flow between eccentric cylinders, the dye structure is independent of the rotation rate of the cylinder (or in the case of both cylinders rotating simultaneously, only dependent on the ratio of angular speeds). As long as the Reynolds and Strouhal numbers are small, the mixing morphology is characterized solely by the displacement of the boundary during a period (Swanson and Ottino, 1990). For a shear-thinning fluid, however, the viscosity is a function of the shear rate. Consequently, for non-Newtonian flow, the speed of the boundaries plays an important role in the dynamics governing the mixing.

Flow geometry and time-periodic operation

The time-periodic flow is simulated in a prototypical geometry of either counterrotating or corotating eccentric cylinders. This geometry has the advantages of smooth boundaries and has been used in a variety of experimental studies in chaotic advection (Chaiken et al., 1986; Swanson and Ottino, 1990). Additionally, an analytical solution exists for Stokes flow in this geometry (Ballal and Rivlin, 1976) and comparisons to a well characterized Newtonian system (Swanson and Ottino, 1990) are possible. The flow geometry is specified by a dimensionless gap μ and a dimensionless eccentricity ϵ which are defined as:

$$\mu = \frac{r_o}{r_i} - 1, \tag{1}$$

$$\epsilon = \frac{e}{r_o - r_i}, \tag{2}$$

The geometry in this study corresponds to $\mu = 2.0$ and $\epsilon = 0.45$.

Chaotic advection is accomplished by a time-periodic forcing of the cylinder boundaries. The wave form is a symmetric, out-of-phase square wave (there are techniques to match other time-periodic wave forms to this one; see Swanson, 1991; Jana et al., 1994). A period, T, is defined by rotation of the inner cylinder for $T/4$, followed by rotation of the outer cylinder for $T/2$, and concluding with a rotation of the inner cylinder for $T/4$. The cylinders are operated either in corotating or counterrotating modes. The respective angular velocities are Ω_i and Ω_o, and the ratio of the angular velocities, Ω_i/Ω_o, is denoted as Ω. The magnitude of Ω is set equal to the ratio of the radii so that the linear speed is the same on both cylinders. A particular time-periodic flow is characterized by the angular displacement of the outer cylinder in a period:

$$\theta = \int_0^T \Omega_o(t)\, dt. \tag{3}$$

Four time-periodic flows are studied: $\theta = 3\pi/2$ and 2π for either counterrotating ($\Omega < 0$) or corotating ($\Omega > 0$) cylinders. The total angular displacement ($\theta_T = \theta N_p$) is kept constant for experiments with different θ values. Since the geometry, streamlines,

and square wave are symmetric, the chaotic patterns formed by the tracer possess a high degree of symmetry at the end of each period.

Mathematical Model and Computational Algorithm

Equation of motion for a shear-thinning fluid

The rheological model used in this study is the Carreau model with a zero infinite-shear-rate viscosity:

$$\eta = \eta_0 \left[1 + (\lambda_c \dot{\gamma})^2\right]^{(n-1)/2} \tag{4}$$

This model has several advantages over the more common power-law equation, $\eta = k\dot{\gamma}^{n-1}$; it does possess a characteristic viscosity and therefore can be made dimensionless. In addition, viscosity-shear-rate curves for most fluids exhibit a low-shear-rate Newtonian plateau and transition region into the power-law region. The Carreau model accounts for both of these considerations. In keeping with the convention in Bird et al. (1987), we define $\dot{\gamma} = \sqrt{(1/2)\,\mathrm{II}}$, and II is the second invariant of the rate-of-strain tensor G [$G = \nabla v + (\nabla v)^T$ and v is the velocity]. The transition region from the Newtonian plateau to power-law region occurs when λ_c is $O(\dot{\gamma}^{-1})$.

The dimensionless form of the equations of motion for the Carreau fluid is:

$$S = \left[1 + (Cr\dot{\gamma})^2\right]^{(n-1)/2} G \tag{5}$$

$$Re\left(Sr\frac{\partial v}{\partial t} + v \cdot \nabla v\right) + \nabla p - \nabla \cdot S = 0 \tag{6}$$

where p is the pressure. The Re number is scaled with the zero-shear-rate viscosity. The Strouhal number, Sr, is the ratio of a convective time scale (L/V) to a characteristic time scale describing the dynamic or unsteady nature of the flow (T_{flow}). For a time-periodic flow such as the ones discussed in this article, a good choice for T_{flow} is the half-period length, $T/2$. This time scale is the duration of either cylinder rotating in the time-periodic wave form described in the previous section. The importance of the transient velocity field is given by the magnitude of $ReSr$. If $ReSr$ is large, then the transient field is important; conversely, if $ReSr$ is small, we can neglect the transient field and approximate the time-periodic flow as a piecewise steady flow. This approximation is discussed further in the section on Integration of the Dynamical System.

Two dimensionless numbers characterize the shear-thinning nature of the flow: the shear index and the Carreau number, $Cr = \lambda_c V L^{-1}$, which can be regarded as a dimensionless shear rate. The transition of the viscosity from Newtonian to power-law behavior occurs when Cr is $O(1)$.

Calculation of the steady-state velocity fields

The simulation of a power-law fluid is a straightforward adaptation of the simulation of the Navier-Stokes equations. The algorithm used in this study is based on a finite difference, method of lines approach (Satofuka, 1986) using the compressible form of the continuity equation. Since the flow equations are simulated using a finite difference algorithm, the spatial domain in the eccentric annulus is discretized with a bipolar coordinate system. The advantage of this coordinate system is that both boundaries of the eccentric cylinders can be specified as a constant value of the radial coordinate.

In a method of lines algorithm, once the spatial derivatives are discretized with finite differences, the PDE is transformed into an ODE in time. The resulting ODE is integrated using a variety of integration routines such as Euler, Runge-Kutta, Gear and Bulirsch-Stoer. In this system, most of the discretization error stems from the resolution of the spatial derivatives, and the ODE systems are integrated using a simple explicit Eulerian algorithm to keep the computation times resonable without a significant loss in accuracy. A more complete description of the numerical algorithm and coordinate system can be found in Niederkorn (1993).

The time integration is continued until steady state is achieved. The criterion used to terminate the integration should be fairly strict since the resulting solution must be of sufficient accuracy to permit the simulation of a chaotic flow. Since it is well established that errors grow exponentially in chaotic advection calculations (Franjione and Ottino, 1987), the criterion should be based on the time frame of the chaotic simulation and an acceptable amount of error in the final solution. Based on these factors, the velocity is assumed to be steady state when the relative change in the velocity field is $O(10^{-5})$. The reason for this choice is also based on the fact that the deviation of the velocity from the Newtonian flow is $O(10^{-2})$, and the error due to the integration truncation should be at least two orders of magnitude less than the physical phenomena that are being modeled. Typical CPU times for calculating the steady-state fields range from 8 to 27 hours on a Digital DEC-station 5000 Model 200 for the range of Cr and n studied.

The algorithm is validated by determining its ability to reproduce the analytical solution for a Newtonian flow. The differences in the discretized steady-state velocity fields are quantified by a root mean-square (rms) deviation:

$$\text{rms} = \sqrt{\frac{1}{N}\sum_{1}^{N}\left(v_{\text{Newtonian}} - v_{\text{non-Newtonian}}\right)^2}, \tag{7}$$

where N is the number of interior nodes. The Newtonian limit is produced in the shear-thinning flow by setting either $Cr = 0$ or $n = 1$. The rms-value for the computed velocity field in this limit is 2.4×10^{-4} on a 49×96 grid. This limit is acceptable and within the discretization error of the grid.

There is also a trade-off in computational resources regarding a more accurate integration method or a finer grid discretization. To determine a suitable combination, computations are also done for a number of grid sizes—25×48, 37×72, and 49×96—with either a first-order (Euler) or second-order (midpoint) integration method. For a given amount of CPU time, a finer grid with the first-order integration produced a more accurate solution than a coarser grid with the second-order interpolation. This result indicates that most of the numerical error is concentrated in the spatial discretization. Consequently, the 49×96 grid with the first-order integration is determined to be the most accurate without requiring excessive computational resources. The computational grid is shown in Figure 1.

Integration of the dynamical system

Once the steady-state velocity fields have been computed,

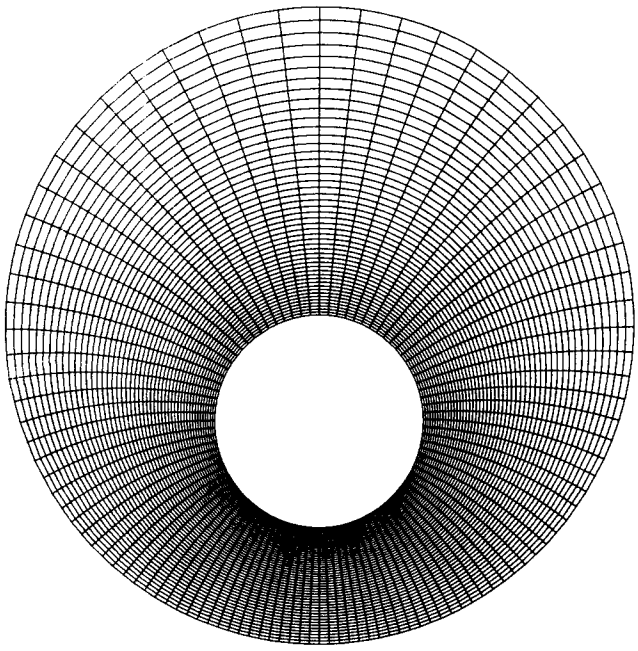

Figure 1. Computational grid in bipolar coordinate frame: 49 x 96 nodes.

the analysis of the chaotic dynamics is based on the integration of the equation:

$$\frac{dx}{dt} = v(x, t); \quad x_{t=0} = X. \tag{8}$$

where v is specified on a finite difference grid. The time dependence of v is the source of the chaotic behavior in the system, and this dependence is periodic and discontinuous since only one cylinder is rotating at a given time. If the characteristic velocity equals the linear velocity of either cylinder and the characteristic length is $r_i\mu$, then Sr can be expressed as:

$$Sr = \frac{\mu}{\theta}\frac{r_i}{r_o}. \tag{9}$$

The periodic flows considered in this article are defined by $\theta = 3\pi/2$ and 2π with a corresponding value of $Sr = 0.14$ and 0.11, respectively. We are also only concerned with slow flows, $Re = 10^{-3}$. Under these conditions, the transient term in the equation of motion is negligible and the time-periodic flow can be considered piecewise steady.

The dynamical system in Eq. 8 is integrated using the steady-state velocity field of either cylinder moving in a periodic manner. The equation is integrated using a second-order Runge-Kutta method with an adaptable time step to prevent a trajectory based on a local velocity from traveling too far out of the local neighborhood before the velocity is updated. Bilinear interpolation is used to calculate the velocity from the nodal values.

The accuracy of the grid and the integration methods for Eq. 8 can be validated by the following comparison. A chaotic tracer advection simulation (described in the next section) is computed using the above integration methods and a discretized form of the analytical solution on the 49×96 grid. This solution is compared to an "exact" solution using the analytical solution and the fourth-order Runge-Kutta integration with adaptable time step (ODEINT from Press et al., 1989). The results indicate that the midpoint integration, bilinear interpolation, and grid are of sufficient accuracy to reproduce the chaotic patterns of the analytical solution.

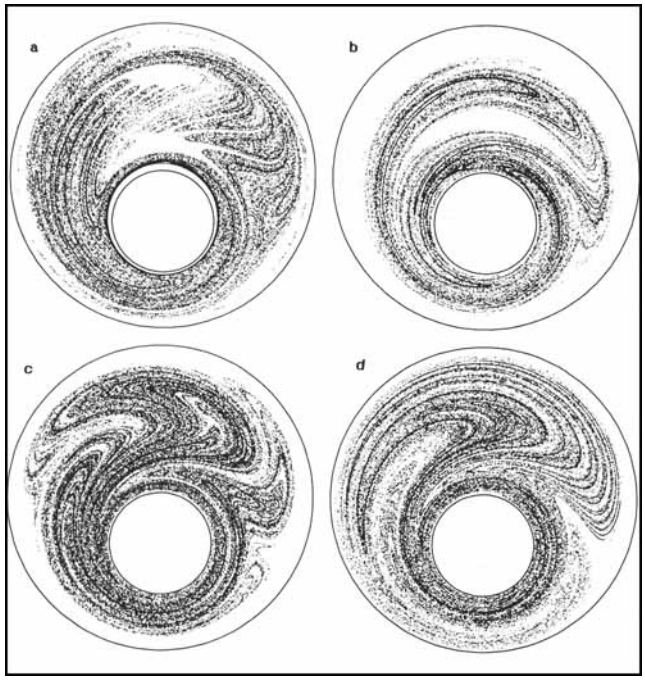

Figure 2. Tracer advection simulations for Newtonian flow.

(a) $\theta = 3\pi/2$ and $\Omega < 0$; (b) $\theta = 2\pi$ and $\Omega < 0$; (c) $\theta = 3\pi/2$ and $\Omega > 0$; (d) $\theta = 2\pi$ and $\Omega > 0$.

Analysis of Time-Periodic Mixing

Tracer advection computation

Many previous experimental studies in chaotic advection (see, for example, Chien et al., 1986; Chaiken et al., 1986; Swanson and Ottino, 1990) have focused on the advection of a passive fluorescent tracer. A typical experiment is performed by injecting a small round tracer of fluid containing the dye and advecting (stirring) the fluid by periodic motion of the boundaries. If the tracer is modeled as a collection of points, the position of the tracer can be computed by integrating the trajectories of all the points. An accurate picture of the structure of the folds after a number of periods can be achieved by plotting *all* the positions corresponding to the previous periods. This type of simulation provides a faithful representation of the experimentally observed dye patterns. An acceptable degree of detail can be achieved by representing the tracer with an array of about 5,000 points. The size and initial location are similar to a typical tracer advection experiment. A typical CPU time for this type of calculation is about 6–8 hours on a Digital DECstation 5000 Model 200.

Tracer advection simulations for the Newtonian fluid are shown in Figure 2 for both counterrotating and corotating flow and $\theta = 3\pi/2$ or 2π. The counterrotating flow for $\theta = 3\pi/2$ is close to a bifurcation in the island structure where an elliptic period-1 point bifurcates into a hyperbolic period-1

point and two elliptic period-2 points resulting in the intricate structure of folds in the large gap in Figure 2a. The counter-rotating flow for $\theta = 2\pi$ is of interest because of the presence of an elliptic period-1 point and the surrounding crescent-shaped island (see Figure 2b). There is also a large regular region adjacent to the outer cylinder in this flow. The co-rotating flows (Figures 2c and 2d) are studied because there are no large low-order periodic islands and the amount of stretching is larger than the corresponding θ for $\Omega < 0$. There is, however, a very thin period-1 island located in the small gap for $\theta = 2\pi$.

Stretching of fluid elements

Efficient fluid mixing is a result of stretching and folding of fluid elements. As the kinematics change due to non-Newtonian flow phenomena, the time scale of the stretching rate should change but remain exponential as long as the flow remains chaotic. The dependence of this time scale provides an important quantitative measure of the impact of the non-Newtonian kinematics on mixing.

This time scale is defined in the following manner. The lineal stretching rate λ is:

$$\lambda = \lim_{dX \to 0} \frac{|dx|}{|dX|}. \tag{10}$$

Since the stretching rate is exponential, the time scale T_c is defined as:

$$<\lambda> = \exp\left(\frac{t}{T_c}\right), \tag{11}$$

and $<\lambda>$ is the geometric mean of the spatially distributed values of λ. The evolution of λ can be calculated from the deformation tensor for the flow (for example, see Swanson and Ottino, 1990). This method is time-consuming, but accurate, for an analytical velocity field. It is, however, less accurate to compute λ with this method for a discretized velocity field, since it requires the evaluation of velocity gradients. A simpler and still reasonably accurate calculation can be done by measuring the distance, d, between two "adjacent" material points as they are separated by the flow. This is equivalent to representing the line segment dX in Eq. 10 by its two end points. An analogous time constant T_c can be extracted from this calculation:

$$<d> = \exp\left(\frac{t}{T_c}\right), \tag{12}$$

where $<d>$ is the geometric mean of the spatially distributed values of d. The results are presented as a normalized time constant, $T_R = T_c / T_{c,\ \text{Newtonian}}$. The computational cost for this method is about 3-4 hours on the DECstation 5000.

Periodic points

The basic structure of the mixing patterns produced by a time-periodic chaotic flow is provided by the location of periodic points. If we consider the flow to be a mapping M in

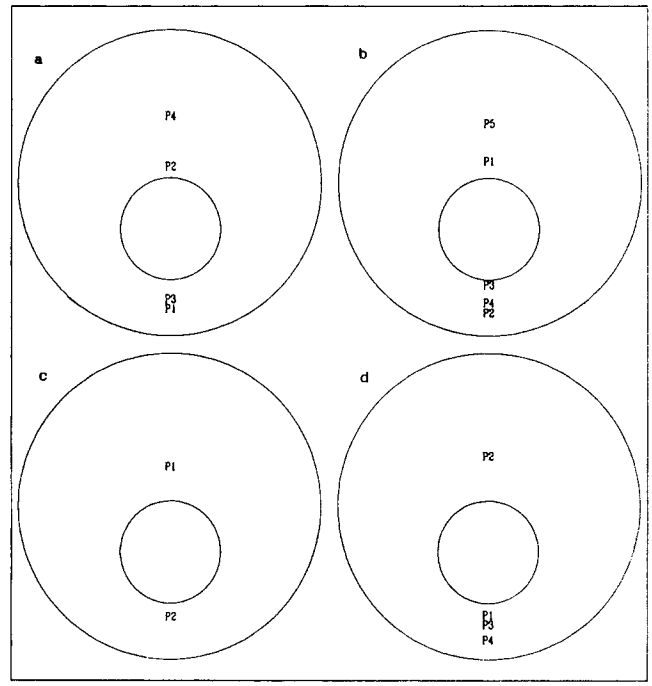

Figure 3. Location of period-1 points for Newtonian flow.
(a) $\theta = 3\pi/2$ and $\Omega < 0$; (b) $\theta = 2\pi$ and $\Omega < 0$; (c) $\theta = 3\pi/2$ and $\Omega > 0$; (d) $\theta = 2\pi$ and $\Omega > 0$.

that all fluid elements get mapped to a new spatial location after each period,

$$\boldsymbol{P}_{i+1} = M(\boldsymbol{P}_i), \tag{13}$$

a periodic point of order m is defined as:

$$\boldsymbol{P}_m = \boldsymbol{P}_0 \quad \text{and} \quad \boldsymbol{P}_{i<m} \neq \boldsymbol{P}_0. \tag{14}$$

For example, a periodic point of order two gets mapped back to its original position after two periods, but not before (otherwise, it would be a period-1 point). Periodic points are classified as either elliptic or hyperbolic depending on the nature of the deformation surrounding the material point. The character of a periodic point is determined by the eigenvalues of the linearized mapping in the neighborhood of the point. Since elliptic points (complex eigenvalues) are associated with islands and hyperbolic points (real eigenvalues) are associated with chaotic regions in the flow, the impact of non-Newtonian kinematics on the quality of mixing can be analyzed by examining the character and location of the periodic points.

The search for the periodic points is facilitated by the symmetry in the flow patterns: the arrangement of the periodic points is symmetric about the geometrical line of symmetry. This is a property of a symmetric geometry and time-periodic wave form and holds as long as the velocity field remains symmetric. The CPU time for the search of the period-1 points assuming symmetric placement is about 30 minutes. The locations of the period-1 points corresponding to the flows in Figure 2 are shown in Figure 3.

There are two manifolds associated with every hyperbolic periodic point: a fluid element travels along the unstable man-

ifold as it leaves the neighborhood of the hyperbolic point, and a fluid element travels along the stable manifold as it approaches the hyperbolic point. Since the maximum amount of stretching occurs along the unstable manifolds, the evolution of these manifolds provides a measure of how the degree of stretching is affected by the non-Newtonian character of the flow. The analysis of the unstable manifolds is not as localized as the information from the eigenvalues of the linearized flow around the hyperbolic periodic points. Initially, the unstable manifold is influenced by the local neighborhood of the periodic point. However, as the unstable manifold evolves and spreads to other regions in the flow domain, it is influenced by other periodic points.

The arc length of the unstable manifold is calculated in the following manner. First, a line of 5,000 equally spaced points is placed along the eigendirection of maximum stretch in the neighborhood of the hyperbolic point. The total length of this initial line is 1% of the average gap width. Second, the points are advected in time, and the length of the manifold is calculated by assuming it is piecewise linear. This assumption is valid as long as the neighboring points are not separated by a large distance. However, because of the exponential stretching along the manifolds, this method is feasible only for a short time ($\theta_T < 6\pi$). Finally, the arc length of the manifold at some time t is normalized to its initial length. The CPU time for computing the unstable manifolds is between 66–125 minutes on the DECstation 5000. The longest unstable period-1 manifold for each of the four time-periodic flows in Figure 2 is illustrated in Niederkorn (1993).

Chaotic Advection of a Shear-Thinning Fluid

The two important flow parameters for the shear-thinning fluid are Cr and n. To explore a reasonable amount of the parameter space, two series of cases are studied: first, n is held constant at 0.5 and Cr is set to 1, 2, 4, and 10; second, Cr is held constant at 4 and n is set to 0.7, 0.6, 0.5, and 0.3. The case for $Cr = 4$ and $n = 0.5$ is common to both series. The series with constant n represents an increase in the dimensionless shear rate and spans the transition region into the power-law region; the series with constant Cr represents an increase in the shear-thinning nature of the fluid and is contained entirely within the power-law region. Throughout this section, these two series will be referred to as "constant Cr" or "$Cr = 4$" and "constant n" or "$n = 0.5$."

Steady flow

Before the chaotic flows are analyzed, it is constructive to examine the steady-state flow with either cylinder rotating since these flows provide the building blocks for the time-periodic flows. Contours of the dimensionless viscosity for the inner cylinder rotating are plotted in Figure 4 for constant Cr. The shear-thinning effect is concentrated near the rotating inner cylinder. In these gray-scale plots, black corresponds to a viscosity less than 0.4 and white corresponds to a viscosity greater than 0.9; the five intermediate levels of gray correspond to 0.1 increment. Contours of the dimensionless viscosity for the outer cylinder rotating are plotted in Figure 5 for constant n. With the outer cylinder rotating, the shear-thinning effect is first noticeable near the stationary cylinder; as Cr increases, the decrease in viscosity is significant throughout most of the

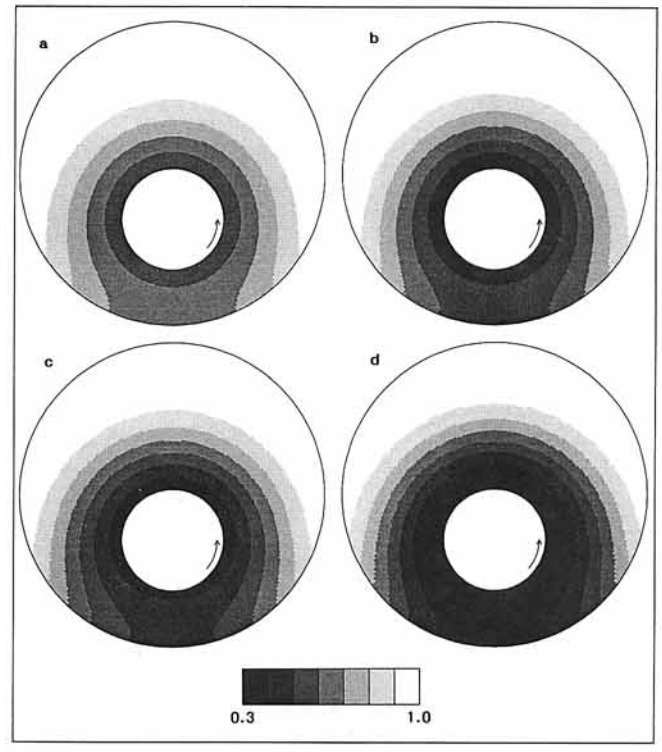

Figure 4. Contours of the viscosity for steady shear-thinning flow with the inner cylinder rotating, $Cr = 4$.

(a) $n = 0.7$; (b) $n = 0.6$; (c) $n = 0.5$; (d) $n = 0.3$.

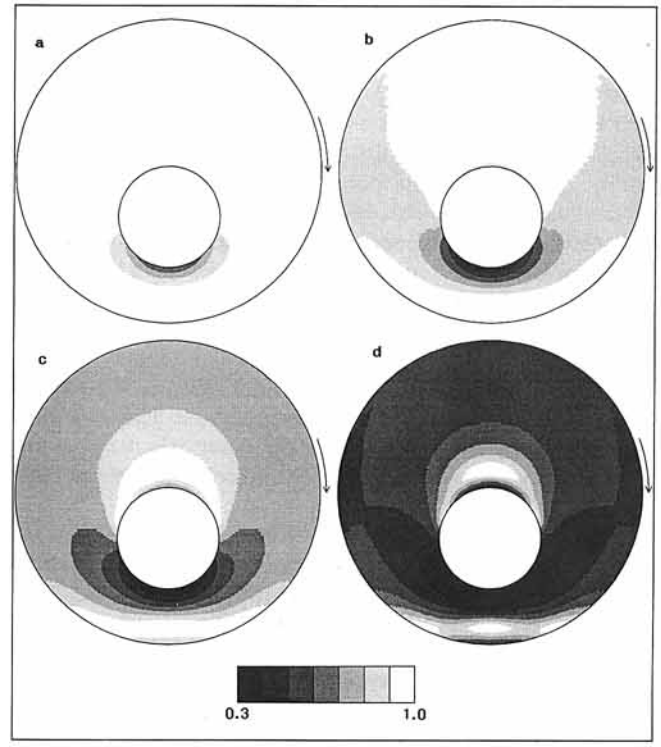

Figure 5. Contours of the viscosity for steady shear-thinning flow with the outer cylinder rotating, $n = 0.5$.

(a) $Cr = 1$; (b) $Cr = 2$; (c) $Cr = 4$; (d) $Cr = 10$.

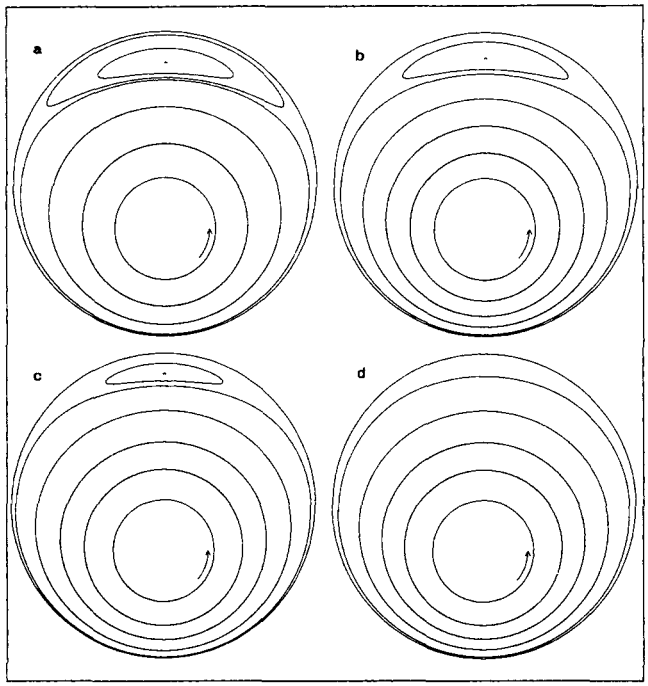

Figure 6. Steady-state streamlines for shear-thinning flow with the inner cylinder rotating, $Cr = 4$.

(a) $n = 0.7$; (b) $n = 0.6$; (c) $n = 0.5$; (d) $n = 0.3$.

flow domain. For either cylinder rotating, the average viscosity varies from 0.8 to 0.3 for constant n and from 0.7 to 0.4 for constant Cr. The trend in the contours is similar for either constant n or constant Cr.

The steady streamlines with the inner cylinder rotating are illustrated in Figure 6 for $Cr = 4$. The separation bubble shrinks and eventually disappears as the fluid becomes more shear-thinning for both constant Cr or n. As the separation bubble shrinks, the two parabolic points associated with the separation streamline move closer to each other and the elliptic point in the center of the bubble moves toward the outer cylinder. The disappearance of the separation bubble represents a bifurcation in the streamline pattern as the two parabolic points and the elliptic point converge to the same point on the outer cylinder and annihilate each other.

The steady streamlines with the outer cylinder rotating are not as nearly affected and not presented here. The separation bubble shrinks only slightly with the outer cylinder rotating. Consequently, there is no observed bifurcation for the outer cylinder rotating.

In all cases of steady flow, the streamlines remain symmetric about the geometrical line of symmetry connecting the centers of the two cylinders. The rms deviation as calculated by Eq. 7 ranges from 6.0×10^{-3} to 2.8×10^{-2} for $n = 0.5$ and from 1.1×10^{-2} to 3.5×10^{-2} for $Cr = 4$. Even though the viscosity varies significantly throughout the spatial domain, the effect on the velocity field is attenuated although there is a significant change in the topology of the steamlines with the inner cylinder rotating. The main question is given the small differences in the steady-state velocity fields: what are the implications on the chaotic dynamics as the steady-state fields are combined in various ways for the periodic flow?

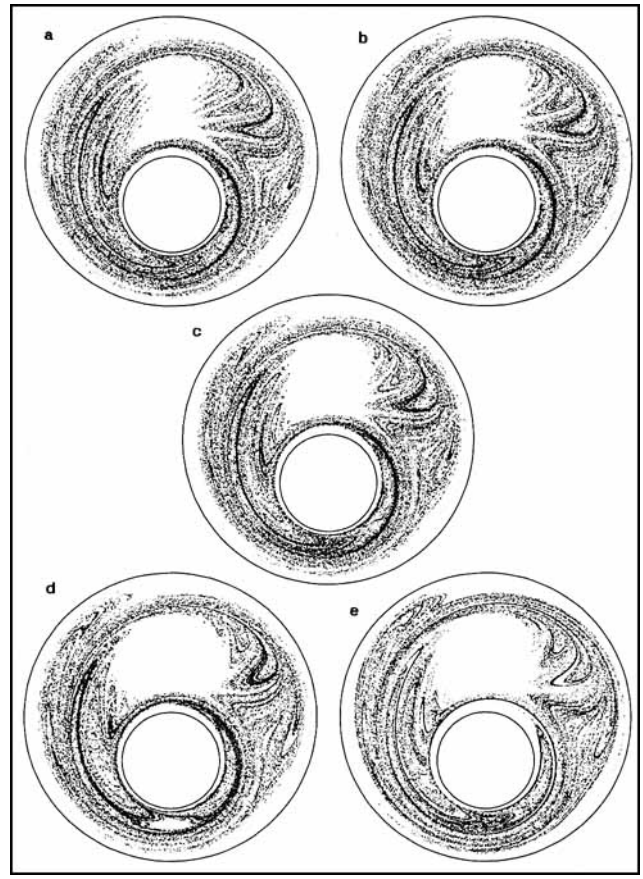

Figure 7. Tracer advection simulations for shear-thinning flow: $\theta = 3\pi/2$ and $\Omega < 0$ (counterrotating).

Figures to the left are for $n = 0.5$ and figures to the right are for $Cr = 4$. The figure in the middle is common to both series. The flow becomes more shear-thinning when starting at the top row and continuing to the bottom row. (a) $Cr = 2$ and $n = 0.5$; (b) $Cr = 4$ and $n = 0.6$; (c) $Cr = 4$ and $n = 0.5$; (d) $Cr = 10$ and $n = 0.5$; (e) $Cr = 4$ and $n = 0.3$.

Birth of period-1 islands

The tracer advection computations for $\theta = 3\pi/2$, $\Omega < 0$, and $N_p = 16$ are shown in Figure 7. In this and the following discussion on periodic flows, the location of the periodic points, P1, P2, and so on (refer to Figure 3 for the locations) does not change significantly since the kinematics do not change significantly. In both series, as the fluid becomes more shear-thinning, the folds retract from the large gap region leaving a large period-1 island around P4 where the tracer does not penetrate. In addition for $Cr = 10$ (Figure 7d), another period-1 island forms around P3 near the inner cylinder in the small gap. The eigenvalues for P3 and P4 are listed in Table 1. The birth of the period-1 islands around P3 and P4 is a result of the eigenvalue of the hyperbolic point decaying to unity and then the point transforming into an elliptic point. The character of P4 is highly sensitive to the shear-thinning effect: the point transforms into an elliptic point at relatively low values of Cr and $1\text{-}n$. This type of transition causes a decrease in the coverage of the tracer and hence a decrease in the amount of mixing in the fluid.

Note the qualitative difference for $n = 0.3$ in Figure 7e; there

Table 1. Eigenvalues of Period-1 Points which Change Type in Counterrotating Flow

	P3, $\theta = 3\pi/2$	P4, $\theta = 3\pi/2$	P5, $\theta = 2\pi$
Newtonian	2.61	1.38	elliptic
$n = 0.5$			
$Cr = 1$	2.50	1.37	elliptic
$Cr = 2$	2.34	1.21	elliptic
$Cr = 4$	1.98	elliptic	elliptic
$Cr = 10$	elliptic	elliptic	1.56
$Cr = 4$			
$n = 0.7$	2.23	1.13	elliptic
$n = 0.6$	2.04	elliptic	elliptic
$n = 0.5$	1.98	elliptic	elliptic
$n = 0.3$	1.71	elliptic	1.34

are large gaps between the folds where the tracer has not entered. This structure reflects an increase in the average striation thickness. In this case, the periodic points with the largest eigenvalues and greatest degree of stretching along their manifolds are no longer period-1. This loss of period-1 hyperbolic points is a second mechanism affecting the quality of mixing in the flow. In summary, the overall effect of a shear-thinning viscosity for this flow is a reduction in the amount of mixing due to two mechanisms: the transformation of hyperbolic period-1 points to elliptic period-1 points and the loss of hyperbolic period-1 points with the largest eigenvalues.

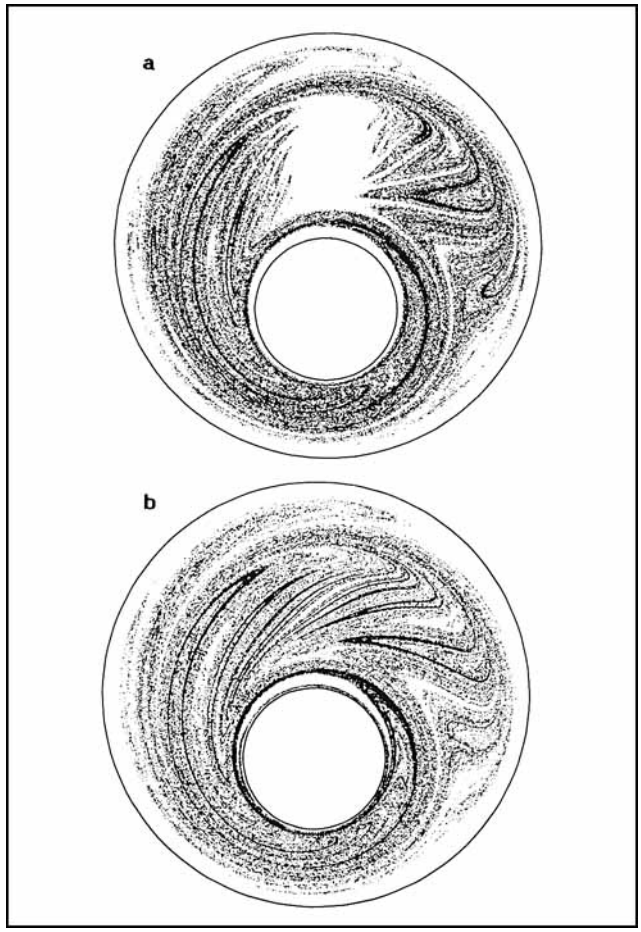

Figure 8. Destruction of period-1 islands, $Cr = 10$ and $n = 0.5$.

(a) $\theta = 19\pi/12$ and $\Omega < 0$; (b) $\theta = 5\pi/3$ and $\Omega < 0$.

Destruction of period-1 islands by changing the operating conditions

Since the transition of hyperbolic periodic points to elliptic points reduces the amount of mixing, it may be possible to manipulate the operating conditions to transform the elliptic periodic points back to hyperbolic. Consider the two period-1 islands in the counterrotating flow for $Cr = 10$ and $n = 0.5$ in Figure 7d. If we manipulate θ and calculate the eigenvalues for P3 and P4, we can determine if and when points P3 and P4 change back to hyperbolic. Indeed for $\theta = 19\pi/12$, P3 is hyperbolic with an eigenvalue of 1.85. The tracer advection simulation in Figure 8a shows that the island surrounding the P3 point has disappeared. The P4 point is still elliptic, but the island surrounding this point is smaller. The computation is for 15 periods, so that the total angular displacement of the outer cylinder (or equivalently the energy input) is the same as for $\theta = 3\pi/2$.

If we further increase θ and measure the eigenvalue for P4, this point changes back to hyperbolic (eigenvalue is 1.20) for $\theta = 5\pi/3$. The tracer advection simulation in Figure 8b shows that the island surrounding P4 has likewise disappeared. This computation is for 14 periods to keep the total angular displacement roughly equivalent. This result indicates that there is nothing inherent in a shear-thinning flow that results in poorer mixing, and careful manipulation of operating parameters can lead to effective mixing in shear-thinning flow. Indeed as we shall see in the next section, the shear-thinning flow can mix more effectively than a Newtonian flow for the same operating conditions.

Collapse of a period-1 island

The tracer advection computations for $\theta = 2\pi$, $\Omega < 0$, and $N_p = 12$ are shown in Figure 9. The crescent shape period-1 island progressively shrinks and eventually disappears as either Cr is increased or n is decreased. Except for the disappearance of this island, the patterns look similar for all values of Cr and n including the thickness of the regular region adjacent to the outer cylinder.

The point P5 is located in the center of the period-1 island which disappears. The eigenvalues for P5 are listed in Table 1. It is interesting that the opposite transition occurs in this flow, the birth of a hyperbolic point with an eigenvalue close to unity from an elliptic point. This type of transition is beneficial to mixing because it results in an increase in the coverage of the tracer.

Once again, the flow for $n = 0.3$ looks qualitatively different. The hyperbolic points P1–3 are no longer period-1. As observed for $\theta = 3\pi/2$, the qualitative difference in the tracer advection simulations occurs in conjunction with the loss of the hyperbolic period-1 points with the largest eigenvalues. This increase in the striation thickness for $n = 0.3$ is more prominent in the corotating flows and is discussed at the end of the next section.

Corotating cylinders

The tracer advection computations for $\theta = 3\pi/2$ and $N_p = 16$

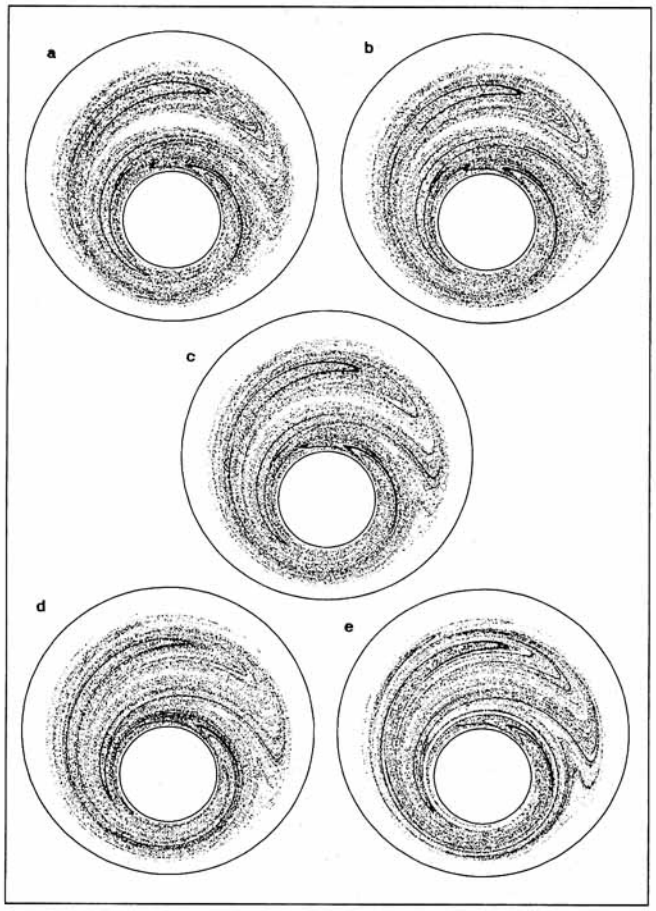

Figure 9. Tracer advection simulations for shear-thinning flow: $\theta = 2\pi$ and $\Omega < 0$ (counterrotating).

(a) $Cr = 2$ and $n = 0.5$; (b) $Cr = 4$ and $n = 0.6$; (c) $Cr = 4$ and $n = 0.5$; (d) $Cr = 10$ and $n = 0.5$; (e) $Cr = 4$ and $n = 0.3$.

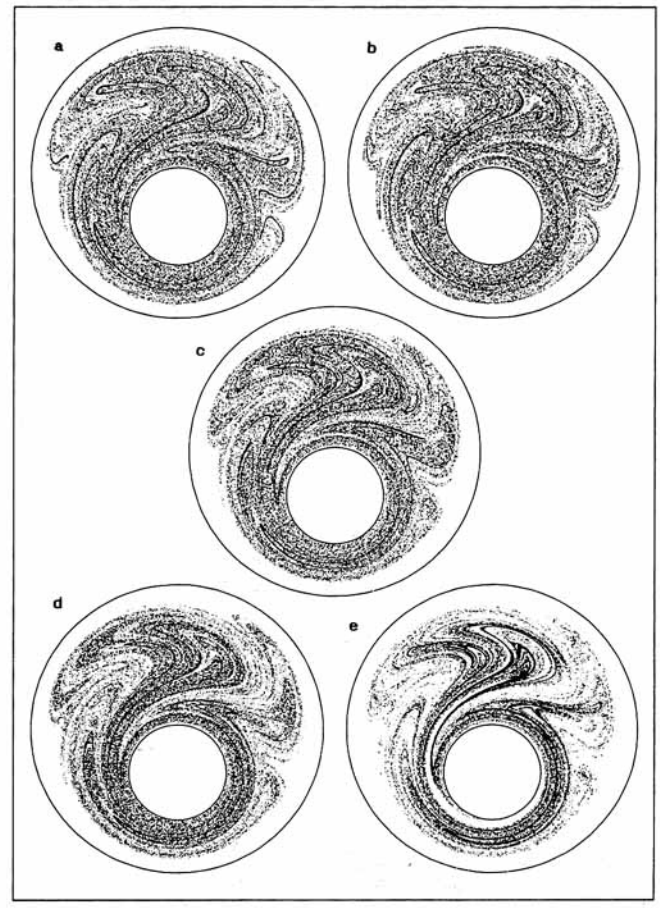

Figure 10. Tracer advection simulations for shear-thinning flow: $\theta = 3\pi/2$ and $\Omega > 0$ (corotating).

(a) $Cr = 2$ and $n = 0.5$; (b) $Cr = 4$ and $n = 0.6$; (c) $Cr = 4$ and $n = 0.5$; (d) $Cr = 10$ and $n = 0.5$; (e) $Cr = 4$ and $n = 0.3$.

are shown in Figure 10. Although, the shear-dependent viscosity seems to have little impact on the asymptotic coverage of the tracer, there is a greater density of points in the region of the "central manifold." This indicates that the rate of stretching is decreasing as the shear-thinning effect increases. For the most part, the flow for $\theta = 2\pi$ and $N_p = 12$ appears largely unaffected by a shear-thinning viscosity. The crescent-shaped period-1 island located around P4 in the small gap widens slightly, and the density of points is lower in the neighborhood of this island. This point initially changes to hyperbolic (eigenvalue is 1.27) for $Cr = 1$ and then back to elliptic as Cr increases and the island widens.

The qualitative difference for $n = 0.3$ and $Cr = 4$ is illustrated in the corotating flow by the tracer advection simulations in Figure 10e. The effects are similar to those observed in the counterrotating flow. Even though the average viscosity is larger in this case than the $Cr = 10$ and $n = 0.5$ case, the dye patterns indicate that a transition occurs betwen $n = 0.5$ and $n = 0.3$ at $Cr = 4$. As with the counterrotating flow, the hyperbolic period-1 points with the largest eigenvalues disappear in the corotating flow (an exception is $\theta = 3\pi/2$ where only P1 disappears, but P2 remains). The differences observed in the simulated tracer advection patterns can be attributed to the loss of the hyperbolic period-1 points associated with high stretching. Due to the loss of high stretching regions, the tracer forms patterns where the "striations" are thicker, and there are bands between the "striations" where the tracer does not penetrate. This type of transition is consequently seen as a barrier to good mixing.

Analysis of period-1 unstable manifolds

If we assume the stretching is dominated by the unstable manifolds of the hyperbolic period-1 points, the sum of the arc lengths of all the significant period-1 manifolds provides a measure of the amount of stretching in the chaotic regions of the flow. The lengths of the longest unstable manifolds are computed for all four time-periodic flows for two periods and $n = 0.5$. The longest manifolds correspond to P1-2 for $\theta = 3\pi/2$ and $\Omega < 0$, P1-3 for $\theta = 2\pi$ and $\Omega < 0$, P1-2 for $\theta = 3\pi/2$ and $\Omega > 0$, and P1 and P3 for $\theta = 2\pi$ and $\Omega > 0$. The relative stretching along the unstable manifolds is computed by normalizing the arc length in the shear-thinning flow to the length in the Newtonian flow.

The relative stretching along the unstable manifolds is shown in Figure 11. The effect on three of the flows is very similar, with the corotating $\theta = 2\pi$ flow being somewhat less affected. This observation suggests that the amount of stretching in the

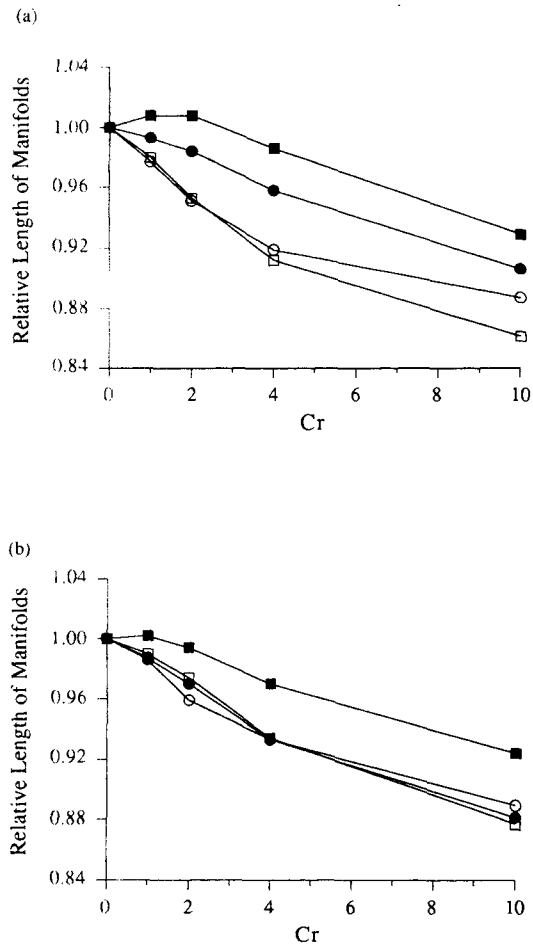

Figure 11. Relative amount of stretching along the unstable manifolds for $n=0.5$.

Circle, $\theta=3\pi/2$ and square, $\theta=2\pi$; open symbol, $\Omega<0$ and filled symbol, $\Omega>0$. (a) 1 period; (b) 2 periods.

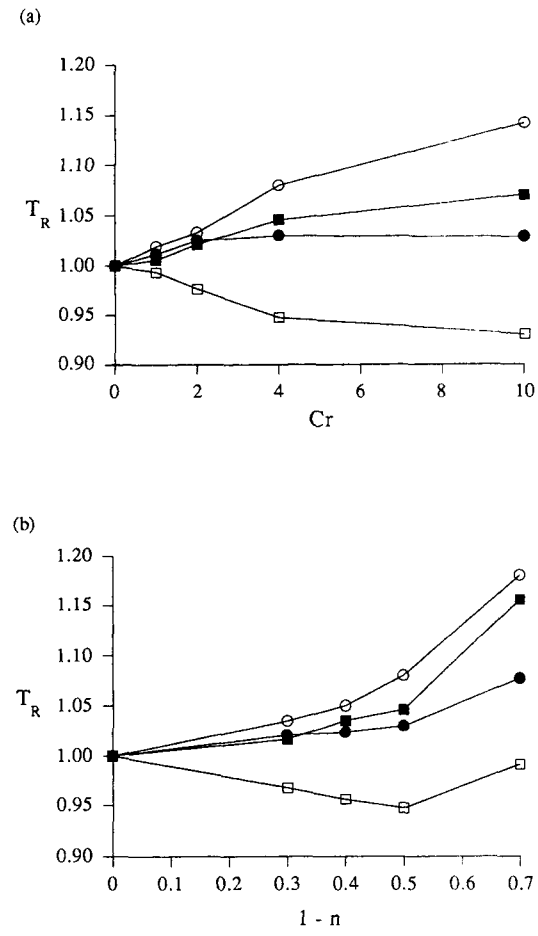

Figure 12. Relative rate of stretching.

(a) $n=0.5$; (b) $Cr=4$. Circle, $\theta=3\pi/2$ and square, $\theta=2\pi$; open symbol, $\Omega<0$ and filled symbol, $\Omega>0$.

chaotic region is decreasing in a similar manner in a number of different flows; this decrease may be common and independent of the operating parameters. However, since these flows demonstrate very different island structures, this method is insensitive to island bifurcations. For example, in the counterrotating flows, the stretching is higher for $\theta=3\pi/2$ at $Cr=10$ even though there are two islands present in this flow and none for the $\theta=2\pi$ flow. The reason for this is that the unstable manifolds only indicate what the effect on stretching is in the chaotic regions only. A more global analysis is needed to detect the presence of islands. This global behavior can be ascertained with a spatial distribution of the rate of stretching throughout the flow domain.

Spatial distribution of the stretching rate

What is the relationship between the stretching rate and the parameters Cr and n? A global average of the rate of stretching is obtained from the time constant for the exponential separation distance (Eq. 12). The relative time constant T_R is plotted in Figure 12 as a function of both Cr and n. A larger time constant indicates that the rate of stretching is decreasing as more time is required to produce the same amount of stretching. The ordering in the two plots is the same: the flow for $\theta=3\pi/2$ and $\Omega<0$ has the largest relative time constant due to the birth of the large period-1 islands, and the flow for $\theta=2\pi$ and $\Omega<0$ has the smallest relative time constant; furthermore, T_R is less than unity for $\theta=2\pi$ and $\Omega<0$ indicating that the relative stretching is increasing as the flow becomes more shear-thinning. This behavior can be attributed to the collapse of the period-1 island in this flow. The island progressively shrinks as Cr increases or n decreases, and in the region of the island, points undergoing linear stretching are being replaced by points undergoing exponential stretching. Even though the stretching is decreasing in other parts of the flow, the transformation of this island is significant enough to increase the overall average of the stretching rate. In addition, once the island disappears, there are no longer competing effects and the slope levels off and begins to increase.

The effect on T_R for the corotating flows is bracketed by the counterrotating flows. There is only a small effect on the rate of stretching in the corotating flow. The fact that there are no island bifurcations in these flows may be part of the reason for the stretching rate to be less affected. In both plots, the time constant for $\theta=2\pi$ is initially less than that for $\theta=3\pi/2$, but the time constant for $\theta=2\pi$ becomes somewhat larger as the flow becomes more shear-thinning. This behavior is most likely due to two observations regarding the $\theta=2\pi$ flow:

the stretching rate increases in the small gap at small Cr because of a larger degree of stretching along the unstable manifold of P1 and the initial collapse of the island around P4. Upon a further increase in Cr, this island widens slightly and the stretching rate near the island decreases. Note also the change in slope for all four flows for $n=0.3$ in Figure 12b. The effect of the loss of the period-1 hyperbolic points can be seen here as a relatively large increase in the time scale of the stretching which produces the qualitative differences seen in the tracer advection simulations.

Summary and Conclusions

A power-law shear-thinning viscosity model is used to analyze the mixing characteristics of a non-Newtonian system. Even though the value of the physical parameters is somewhat restricted ($Cr \leq 10$ and $n \geq 0.3$) and the root-mean deviation from Newtonian flow of the steady-state velocity fields is small (less than 4%), large effects are observed in the chaotically advected patterns in the periodic flow. In general, the overall effect of a shear-thinning viscosity is a decrease in the amount of mixing, in both rate and extent. Contrary to common wisdom, however, there are cases ($\theta = 2\pi$ and $\Omega < 0$) where the mixing initially improves. Results are presented in terms of tracer advection simulations, the character of periodic points, amount of stretching along the unstable manifold, and the stretching rate of fluid elements.

A shear-thinning viscosity results in a decrease in the amount of stretching in the flow which is the primary route to efficient mixing. We identify two mechanisms which cause this adverse decrease in stretching. First, periodic hyperbolic points are transformed into periodic elliptic points. This type of mechanism also decreases the asymptotic coverage of a tracer because of the associated birth of regular regions or islands around the periodic elliptic point into which the tracer cannot penetrate. In the one flow where the stretching actually increased for non-Newtonian flow, the opposite transition is observed: the creation of a hyperbolic periodic point from an elliptic periodic point. The second mechanism is the loss of the period-1 hyperbolic points with the largest eigenvalues or the largest amount of stretching along their associated unstable manifolds. This type of mechanism causes an increase in the average striation thickness, but is not as obstructive to efficient mixing since the asymptotic coverage is less affected.

The character of the periodic points is informative by indicating the occurrence of island bifurcations. The scaling of the manifolds indicates that the reduction in the amount of stretching in the chaotic regions is somewhat similar for different operating conditions although one flow scales differently than the other three. The time constant of the stretching rate illustrates the global effect of non-Newtonian fluid properties including the presence of island bifurcations.

Several extensions of the results presented here come to mind. The apparent general decrease in the amount of stretching along the unstable manifolds should be confirmed for other flows and larger number of periods: more time (five-six periods) may be needed to better determine the effect of a shear-thinning viscosity on the development of the unstable manifolds. This requires an adjustable algorithm (Hobson, 1993) to inject points as they are needed to resolve the manifold due to exponential stretching along the manifolds. A brute force computational method of *initially* representing the manifold as a line segment of *equally* spaced points results in prohibitive CPU times and is extremely inefficient, since some parts of the line segment could easily require more orders of magnitude of points to resolve the manifold than others. The study of periodic points should be extended to higher-order periodic points as it is likely that there may be additional manifolds from higher-order points which contributed significantly to the amount of stretching. For a discussion on these issues, see Jana et al. (1994).

It should be emphasized that even though we can successfully model these chaotic flow systems, it is clear that we do not fully understand them. For example, we can identify certain transitions which cause a decrease in mixing, but we still cannot predict *a priori when* these types of transitions will occur. This type of analysis will require a development of a theory of large perturbations in dynamical systems. It is, however, clear from this study of non-Newtonian flows that neglecting the fluid rheology in studying the kinematics of mixing equipment can result in misleading conclusions about design parameters. The ability to model the quality of mixing in non-Newtonian systems will increase with the understanding of the kinematics and chaotic dynamics of the resulting particle paths. These developments can be applied to both experimentally or numerically obtained velocity fields. With the development of faster computers and sophisticated finite-element schemes (Perng and Murthy, 1993; Avalosse et al., 1992) and boundary-fitted finite-difference methods (Papathanasiou and Kamal, 1990) for complicated time-dependent geometries, we are fast approaching the ability to simulate the complicated flow present in process mixing equipment.

Acknowledgment

The authors acknowledge the support of the Department of Energy, Office of Basic Energy Sciences.

Notation

Cr = Carreau number
d = separation distance
dx = infinitesimally small fluid line
dX = initial infinitesimally small fluid line
e = eccentricity of the cylinder
k = consistency index
L = characteristic length scale
n = shear index
N_p = number of periods
r_i = radius of inner cylinder
r_o = radius of outer cylinder
Re = Reynolds number
S = extra-stress tensor
Sr = Strouhal number
t = time
T_R = normalized exponential time scale
v = velocity
V = characteristic velocity
x = coordinate vector
X = initial location

Greek letters

$\dot{\gamma}$ = scalar measure of the rate-of-strain tensor
η = viscosity
η_0 = zero-shear-rate viscosity
λ_c = time constant
θ = angular displacement of outer cylinder/period
θ_T = total angular displacement of outer cylinder
Ω = angular velocity ratio

Literature Cited

Aref, H., "Stirring by Chaotic Advection," *J. Fluid Mech.*, **143**, 1 (1984).

Avalosse, T., M. Crochet, A. Fobelets, and C. Dehennau, "Numerical Simulation of Mixing," *Theoretical and Applied Rheology*, P. Moldenaers and R. Keunings, eds., Elsevier Science Publishers, Amsterdam, 318 (1992).

Ballal, B. Y., and R. S. Rivlin, "Flow of a Newtonian Fluid Between Eccentric Rotating Cylinders: Inertial Effects," *Arch. Rat. Mech. Anal.*, **62**, 237 (1976).

Bird, R. B., R. C. Armstrong, and O. Hassager, *Fluid Mechanics: 1. Dynamics of Polymeric Liquids*, 2nd ed., Wiley, New York (1987).

Carreau, P. J., J. Paris, and P. Guérin, "Mixing of Newtonian and Non-Newtonian Liquids: Screw Agitator and Draft Coil System," *Can. J. Chem. Eng.*, **70**, 1071 (1992).

Chaiken, J., R. Chevray, M. Tabor, and Q. M. Tan, "Experimental Study of Lagrangian Turbulence in a Stokes Flow," *Proc. Roy. Soc. A*, **408**, 165 (1986).

Chien, W.-L., H. Rising, and J. M. Ottino, "Laminar Mixing and Chaotic Mixing in Several Cavity Flows," *J. Fluid Mech.*, **170**, 355 (1986).

Ford, D. E., and J. Ulbrecht, "Influence of Rheological Properties of Polymer Solutions upon Mixing and Circulation Times," *Ind. Eng. Chem., Process Des. Dev.*, **15**, 321 (1976).

Franjione, J. G., and J. M. Ottino, "Feasibility of Numerical Tracking of Material Lines and Surfaces in Chaotic Flows," *Phys. of Fluids*, **30**, 3641 (1987).

Godleski, E. S., and J. C. Smith, "Power Requirements and Blend Times in the Agitation of Pseudoplastic Fluids," *AIChE J.*, **8**, 617 (1962).

Hall, K. R., and J. C. Godfrey, "Power Consumption by Helical Ribbon Impellers," *Trans. Instn. Chem. Engrs.*, **48**, T201 (1970).

Harnby, N., M. F. Edwards, and A. W. Nienow, *Mixing in the Process Industries*, 2nd ed., Butterworth-Heinemann, Oxford (1992).

Hobson, D., "An Efficient Method for Computing Invariant Manifolds of Planar Maps," *J. of Comp. Phys.*, **104**, 14 (1993).

Jana, S. C., G. Metcalfe, and J. M. Ottino, "Experimental and Computational Studies of Mixing in Complex Stokes Flows: The Vortex Mixing Flow and Multicellular Cavity Flows," *J. Fluid Mech.*, **269**, 199 (1994).

Lawal, A., D. H. Kalyon, and Z. Ji, "Computational Study of Chaotic Mixing in Corotating Two-Tipped Kneading Paddles: Two-Dimensional Approach," *Poly. Eng. Sci.*, **33**, 140 (1993).

Leong, C.-W., and J. M. Ottino, "Increase in Regularity by Polymer Addition During Chaotic Mixing in Two-Dimensional Flows," *Phys. Rev. Lett.*, **64**, 874 (1990).

Metzner, A. B., and R. E. Otto, "Agitation of Non-Newtonian Fluids," *AIChE J.*, **3**, 3 (1957).

Middleman, S., *Fundamentals of Polymer Processing*, McGraw Hill, New York (1977).

Niederkorn, T. C., "Chaotic Mixing of Non-Newtonian Fluids in Time-Periodic Flow," PhD Diss., Northwestern Univ. (1993).

Niederkorn, T. C., and J. M. Ottino, "Mixing of a Viscoelastic Fluid in a Time-Periodic Flow," *J. Fluid Mech.*, **256**, 243 (1993)

Nienow, A. W., and T. P. Elson, "Aspects of Mixing in Rheologically Complex Fluids," *Chem. Eng. Res. Des.*, **66**, 5 (1988).

Ottino, J. M., *The Kinematics of Mixing: Stretching, Chaos, and Transport*, Cambridge University Press, Cambridge (1990).

Ottino, J. M., F. J. Muzzio, M. Tjahjadi, J. G. Franjione, S. C. Jana, and H. A. Kusch, "Chaos, Symmetry, and Self-Similarity: Exploiting Order and Disorder in Mixing Processes," *Sci.*, **257**, 754 (1992).

Ottino, J. M., and R. Chella, "Laminar Mixing of Polymeric Liquids," *Poly. Eng. Sci.*, **23**, 357 (1983).

Papathanasiou, T. D., and M. R. Kamal, "Use of Boundary-Fitted Curvilinear Coordinates for the Numerical Simulation of Complex Viscoelastic Flow," *J. Non-Newtonian Fluid Mech.*, **37**, 139 (1990).

Perng, C.-Y., and J. Y. Murthy, "A Sliding-Mesh Technique for Simulation of Flow in Mixing Tanks," *Mixing XIV Conf.*, Santa Barbara, CA (1993).

Press, W. H., B. P. Flannery, S. A. Teukolsky, and W. T. Vetterling, *Numerical Recipes: The Art of Scientific Computing*, Cambridge University Press, Cambridge (1989).

Rauwendaal, C., *Mixing in Polymer Processing*, Marcel Dekker, New York (1991).

Satofuka, N., "Method of Lines Approach to the Numerical Solution of Fluid Dynamic Equations," *Int. Conf. on Numerical Methods in Fluid Dynamics*, F. G. Zhuang and Y. L. Zhu, eds.; *Lecture Notes in Physics*, W. Beiglbock, ed., No. 264, Springer-Verlag, Berlin, 57 (1986).

Swanson, P. D., and J. M. Ottino, "A Comparative Computational and Experimental Study of Chaotic Mixing of Viscous Fluids," *J. Fluid Mech.*, **213**, 227 (1990).

Swanson, P. D., "Regular and Chaotic Mixing of Viscous Fluids in Eccentric Rotating Cylinders," PhD Diss., Univ. of Massachusetts (1991).

Tadmor, Z., and C. G. Gogos, *Principles of Polymer Processing*, Wiley, New York (1979).

Manuscript received Nov. 9, 1993, and revision received Mar. 28, 1994.